# X-RAY TEXTURE ANALYSIS OF CVD DIAMOND

by

Peter Walker, B.S.

A thesis submitted to the Graduate Council of
Texas State University in partial fulfillment
of the requirements for the degree of
Master of Science
with a Major in Physics
May 2018

Committee Members:

Mark Holtz, Chair

Edwin Piner

Alexander Zakhidov

## FAIR USE AND AUTHOR'S PERMISSION STATEMENT

### Fair Use



### Duplication Permission

## ACKNOWLEDGEMENTS

I would like to thank my committee members Dr. Edwin Piner, and Dr. Alexander Zakhidov for their guidance and advice, with special thanks Dr. Mark Holtz for his unwavering patience and support. I would like to thank Raju Ahmed for his substantial contributions to the diamond growths. I would like to acknowledge my colleagues Anwar Siddique, Dr. Sandeep Sohal, and Dr. Mohammed Nazari for their professional support and technical expertise. I would like to thank Texas State University, The Army Research Office, and the Defense Advanced Research Project Agency for financial support.

## TABLE OF CONTENTS

**Page**

## LIST OF TABLES

**Figure** **Page**

## LIST OF FIGURES

**Figure** **Page**

## LIST OF ABREVIATIONS

| Abbreviation | Description |
|---|---|
| ODF | Orientation Distribution Function |
| MTEX | MatLab based Texture Analysis Toolbox |
| HF CVD | Hot filament chemical vapor deposition |
| TD | Transverse Direction |
| RD | Rolling Direction |
| MRD | Multiples of a Random Distribution |

# I. INTRODUCTION

Diamond is an important functional material and has enjoyed a growing number of applications for its extreme material properties. For diamond films produced by chemical vapor deposition, many properties have been found to be dependent on the crystallographic direction of the diamond lattice [1,2], such as roughness, wear resistance [3], optical properties [4]. Under some models, thermal conductivity is predicted to vary with lattice direction[5,6]. The preferred orientation has been shown to vary strongly with the growth parameters such as methane concentration, temperature and pressure [1]. Understanding the orientation distributions of the crystallites is key to describing the full properties of the film.

The orientation distribution is a probability density function that provides the likelihood that a grain in a polycrystalline sample has a given orientation. It cannot be measured directly, and is instead calculated using data from x-ray diffraction, electron backscatter diffraction, or transmission electron microscopy. A method for calculating a function for the orientation distribution was first solved by Bunge in 1967 [7], and can now be quickly obtained using modern software.

In this work, the orientation distribution function (ODF) is found using x-ray diffraction measurements for diamond films under varying methane concentration and thicknesses. The data from the x-ray measurements are analyzed using MTEX, a MATLab based toolbox. A review of texture analysis in CVD diamond and the modern analytic tools will also be provided.

## II. BACKGROUND

### 2.1 Texture

Texture, or preferred orientation, is a description of the alignment of crystal grains in a thin film. Their alignment or partial alignment towards a direction can greatly influence bulk material properties, and films may be tailored through their growth parameters to enhance or diminish the texture [2]. In general, for any polycrystalline film, the orientations of the crystallites evolves through a number of stages starting with island growth, coalescence and further thickening [1].

Following in the description by Bunge [7], let $K_A$ be the fixed sample coordinate system, and $K_B$ be the set of crystal coordinates in the material. Below we can see a sketch of crystallites with different orientations $K_B$ embedded in the sample.

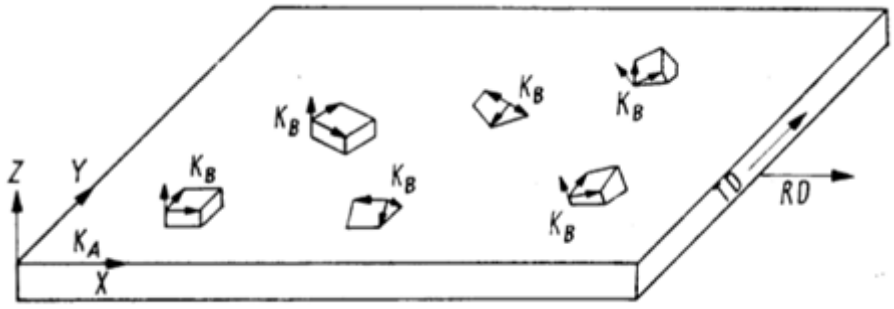


**Figure 1:** Schematic representation of crystallites randomly oriented in a sheet. [7]

Many studies find a particular crystallographic direction ***hkl*** to be preferentially oriented with a direction in the sample reference frame $K_A$ . Moreover, in a large majority of studies, this direction coincided with the substrate normal [2]. This is the *fiber texture*, with the crystal planes ***hkl*** aligned along the *fiber axis* the sample normal. The crystal

orientation $K_B$ is described by three angles that transform it from the frame $K_A$. The Euler angles are employed most commonly for the description of texture.

The directions TD and RD seen in Figure 1 are the Transverse and Rolling Directions. These, together with the Normal Direction (ND), form a set of three orthogonal directions. These sample directions are used due to the early association of texture analysis in the processing of metals such as cold rolling. For polycrystalline films, the RD and TD do not have the same meaning because of the lack of directional processing techniques, and the texture along the two directions is often the same in the case of a fiber texture. Instead, the RD and TD specify two in-plane directions for the sample surface, and the ND is just the sample normal.

### 2.2 Euler Angles

The Eulerian angles are a coordinate system for the description of a rigid body in three-dimensional space in relation to a fixed coordinate system. Other representations such as the matrix, Rodrigues vectors, and quaternions have some advantages in the mathematical treatment of the orientation distribution [7], however the Euler angles are most commonly used for discussing the ODF.

The three Euler angles are denoted many ways; here they will be given as $(\phi_1, \Phi, \phi_2)$. The series of rotations can be described as: (1) A first rotation $\phi_1$ about the z direction, transforming the system $xyz$ to the system $x'y'z$, (2) A rotation $\Phi$ around the $x'$ direction, transforming the system $x'y'z$ to $xy''Z$, (3) A rotation $\phi_2$ around the $Z$ direction, transforming the system to $XYZ$. This can be seen in Figure 2a.

It's important to note that the order of the rotations matter. The initial sample frame can be considered $xyz$, with subsequent frames $x'y'z,\ x'y''z'$ and $XYZ$ as the final crystal frame. The

transformation from the sample frame $xyz$ to the crystal frame $XYZ$ is then described by the rotation:

$$g = \{\phi_1, \Phi, \phi_2\} \quad (1)$$

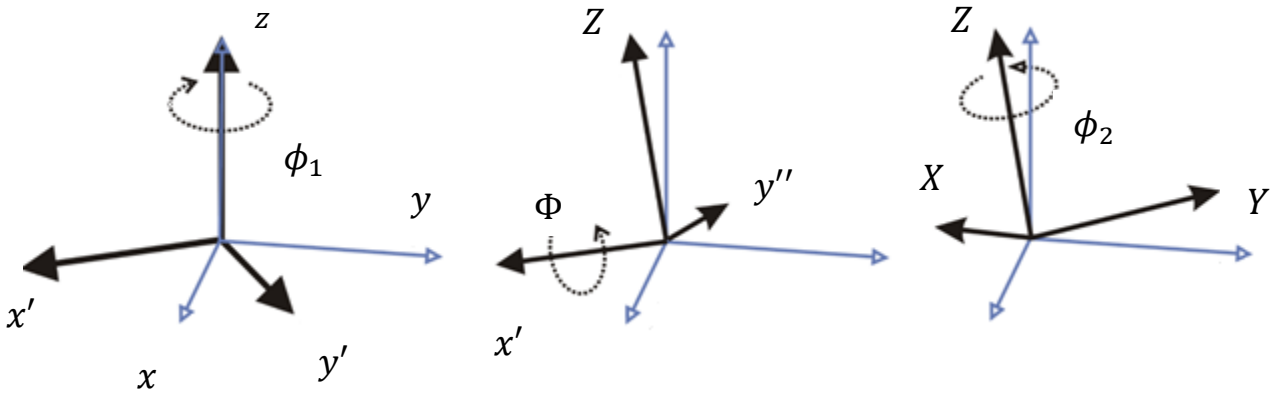


**Figure 2a:** Intrinsic rotations. The rotations occur on each new orientation of the rotating frame.

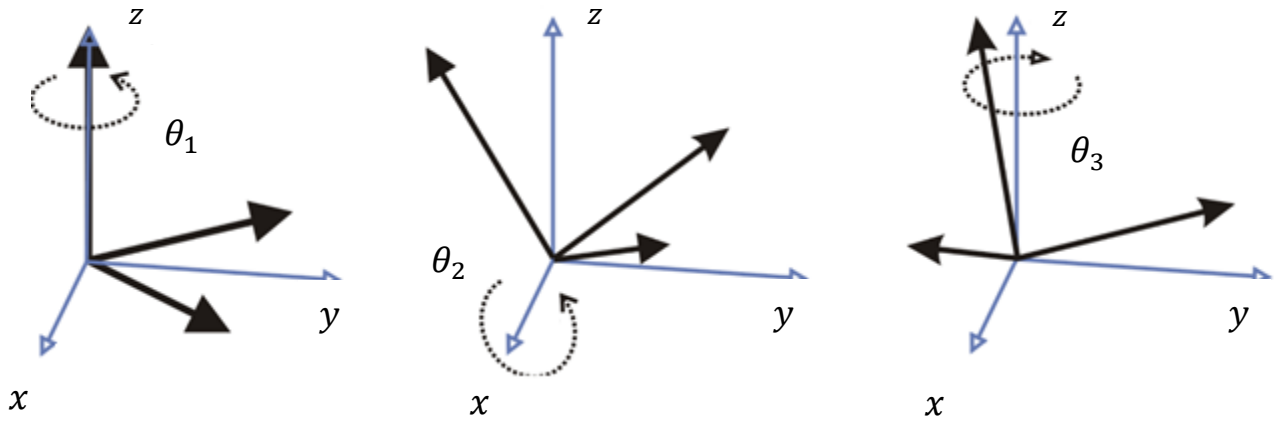


**Figure 2b** : Extrinsic rotations. The rotations occur in reference to the non-rotating frame.

The Euler angles are composed of three intrinsic rotations, meaning that they occur on the body of the rotating coordinate system, not the fixed sample coordinate system. The difference between intrinsic and extrinsic rotations can be seen below in Figure 2. The Euler angles (top) are given in terms of the rotations $\phi_1$, $\Phi$ and $\phi_2$ in that order, while the extrinsic rotations (bottom) are given by arbitrary rotations $\theta_1, \theta_2, \theta_3$.

For the Euler angles, it's worth noting that one rotation occurs around z, and one occurs around Z. In this way, it may help to consider the rotation from the sample frame $K_A$ to a crystal frame $K_B$ as "setting" the Z coordinate, and then rotating around Z through the in-plane directions.

**2.3 Orientation Distribution**

The orientation distribution function is a statistical description of the orientations of the crystallites. The ODF is a probability density, and it describes the volume fraction of crystallites with a given orientation $\{\phi_1, \Phi, \phi_2\}$ relative to a perfectly random distribution. If crystallites with orientation $g$ and a spread of orientations $dg$, are contained within the volume element $dV$, then an probability distribution function $f(g)$ that describes the density of crystallites can be defined by

$$\frac{dV}{V} = f(g)dg \tag{2}$$

To every position $g(\phi_1, \Phi, \phi_2)$ there is a volume fraction of crystallites described by $f(g)$ [7]. The space spanned by the 3 angles $\{\phi_1, \Phi, \phi_2\}$ is the orientation space and is defined between $0 \leq \phi_1, \phi_2 \leq 360°$ , and $0 \leq \Phi \leq 180°$. One way this density function is visualized is by inscribing the ranges of each angle onto the Cartesian coordinates of a cube as seen in Figure 3. The regular x, y, and z coordinates now correspond to the three angles, and a heat map, or contour lines can describe the density at each location.

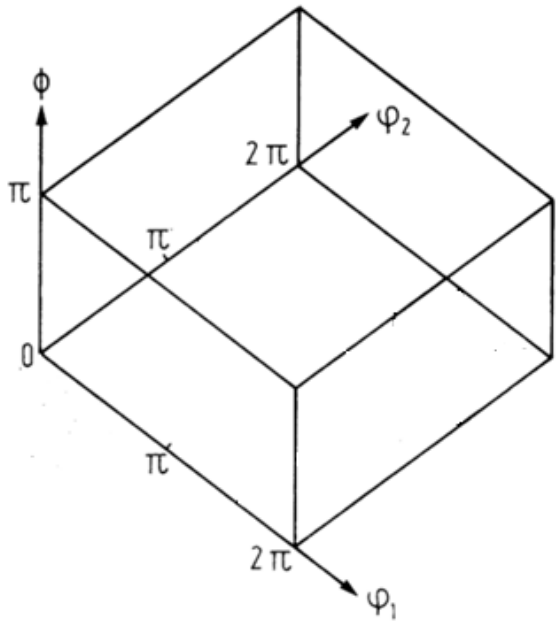


**Figure 3:** The Euler Space. A particular ***hkl*** may be described a coordinate $(\phi_1, \Phi, \phi_2)$ [7]

To see inside the volume of the cube, cross sections are taken of the Euler space so that in each slice two coordinates are varied, and one coordinate is constant for each given slice. It's typical to allow $\phi_1$ and $\Phi$ to vary within the slice, and for $\phi_2$ to remain constant. The $\phi_2$ coordinates then varies with 5° degree changes between slices. One such slice can be seen below in Figure 4. It is common to display 19 panels in a 5x4 display when showing the ODF, allowing $\phi_2$ to vary between 0° and 90°, with the last panel providing information about the set.

The orientation distribution has units of multiples of a random distribution, or MRDs. The MRD is a relative measure that describes textures in reference to a sample with perfectly random crystallites. A sample that has perfectly random crystallites would have a constant value of 1 everywhere. A value of 2 at a given orientation would indicate that the density of crystallites oriented in that direction is twice as would be expected in the random case. A sample approaching

a perfect single crystal would have one emerging orientation and some indistinguishable orientations based on symmetry. If a single crystal cubic system has its (001) direction aligned with the sample normal, and if the (100) is aligned with either the transverse or rolling directions (i.e., the sample and crystal frames are aligned), the MRD value diverges to infinity as the angles $\phi_1, \Phi, \phi_2 \rightarrow 0$.

### 2.3.1 Invariant Measure

One consideration for the normalization of the MRD units is the invariant measure, and how a sample with random crystallites would actually look in in the orientation space. See Figure 4 below

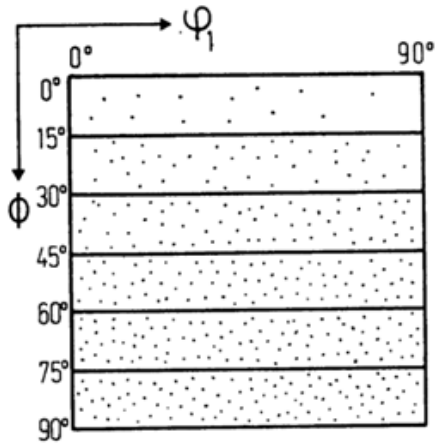


**Figure 4:** A perfectly random sample in orientation space with no corrections. [7]

The reason the distribution looks skewed is because low angles of Φ are points near the poles, and high values of Φ are points near the equator. Equal angle elements of the Euler angles $(\phi_1, \Phi, \phi_2)$ produce unequal area elements in real space where the crystallites are measured. If we were to imagine our x-ray detector moving in a sphere around the sample, the area on the sphere swept out by Φ angles near the equator is much larger than that of the area swept near the poles. To correct for this, Bunge gives the invariant measure as:

$$I(\phi_1, \Phi, \phi_2) = \sin\Phi \tag{3}$$

This allows for an orientation space where a random distribution is represented by a constant density everywhere[7]. If we consider the orientation element $dg$, it must also be scaled by the factor $\frac{1}{8\pi^2}$ for the integration of the three angles over their respective ranges. We obtain a factor $1/2\pi$ for each the integrations of $\phi_1$ and $\phi_2$ over the range of 0 to $2\pi$, and a factor of 2 from integrating $\sin\Phi$ from 0 to $\pi$. The orientation element is given by

$$dg = \frac{1}{8\pi^2} sin\Phi d\phi_1 d\Phi d\phi_2 \tag{4}$$

Combining with (2) we obtain the normalization condition

$$\frac{dV}{V} = \frac{1}{8\pi^2} f(g) sin\Phi d\phi_1 d\Phi d\phi_2 \tag{5}$$

Following this scaling, a random distribution now produces a constant value of 1 everywhere in the orientation space.

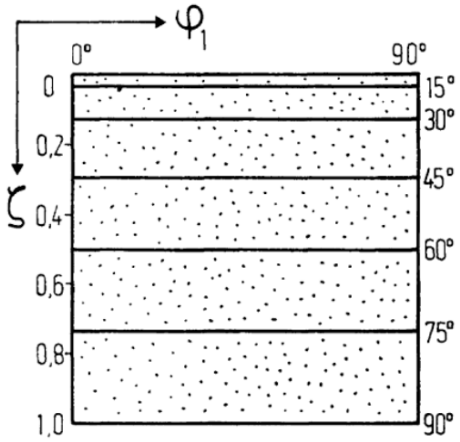


**Figure 5:** A perfectly random sample in orientation space with $\zeta = \sin\Phi$. [7]

## 2.4 Pole Figure Measurement

The pole figure measurement is the fundamental scan in x-ray diffraction for texture analysis. It is performed by maintaining a single Bragg condition between the source and detector for a set of planes $\boldsymbol{hkl}$, and tilting the sample through all orientations in the top hemisphere. Here, we will use the angles typical in x-ray analysis for pole figures. The angle $\alpha$ represents the tilt of the scattering vector $K$ from the unit normal and is bounded between 0 and $\frac{\pi}{2}$. The angle $\beta$ represents the rotation of the vector $K$ around the unit normal and has bounds 0 to $2\pi$. Scanning with a single Bragg condition over all tilts, i.e. the full ranges of $\alpha$ and $\beta$, provides diffraction intensities which can be related to the density of crystallites.

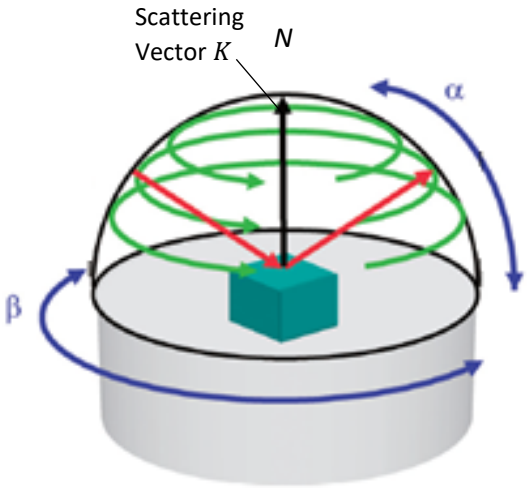


**Figure 6:** Schematic representation of the pole figure measurement. [8]

The intensities, $I_{hkl}(\alpha, \beta)$ are measured for each tilt of the scattering vector. Please note that the labels $(\chi, \phi)$ and $(\psi, \phi)$ may be used for $(\alpha, \beta)$ in some texts. Flat circular projections are generally used to represent the obtained data, and there exist a few possibilities for projecting the function $I_{hkl}(\alpha, \beta)$ onto a unit circle when scaling the angle $\alpha$ to the radial distance in the graph. It is most common to use the stereographic projection for pole figures although the "iso-tilt" and

equal area maps are also used. The Figure 7(a) below relates with Figure 6 from above, and shows two ways the scattering vector at a point P may be projected onto a flat plane through the equator. The two circular, flat, projections on the equator are the subsequent Figures 7(b,c). Values can become tightly packed for high angles of $\alpha$ in the perpendicular projection of Figure 7(b), so other projection schemes such as the stereographic projection, $\tan\frac{\alpha}{2}$, are used for better clarity.

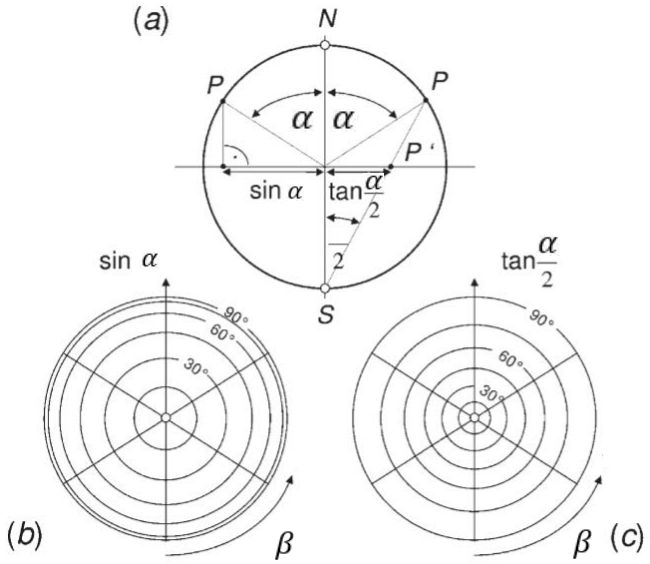


**Figure 7:** (a) Scaling of a point P to P' using perpendicular ($\sin\alpha$) and stereographic ($\tan\frac{\alpha}{2}$) projections, with (b) and (c) as their corresponding nets. [2]

The choice of one net over another depends on preference, but it should be stated what choice of projection is selected. Here, the stereographic projection will be used.

It should be stated that during tilting in the pole figure measurement, different depths of the film are interrogated, and thus an average is produced over the measured penetration depth [2].

Most textures have been shown to increase with thickness, and may produce challenges if information is desired from a particular thickness regime.

### 2.4.1 Interpretation of Pole Figure Measurements

Pole figure measurements on their own can produce very useful qualitative data about the nature of polycrystalline growths by seeing how the positions of the intensities align with the sample reference frame. Most polycrystalline films exhibit a fiber texture aligning with the unit normal of the sample[2], and this can be clearly seen from pole figures without a quantitative analysis of the intensities. If we consider a single crystal sample with the (001) direction aligned with the ND, we can project the other crystallographic directions in the stereograph.

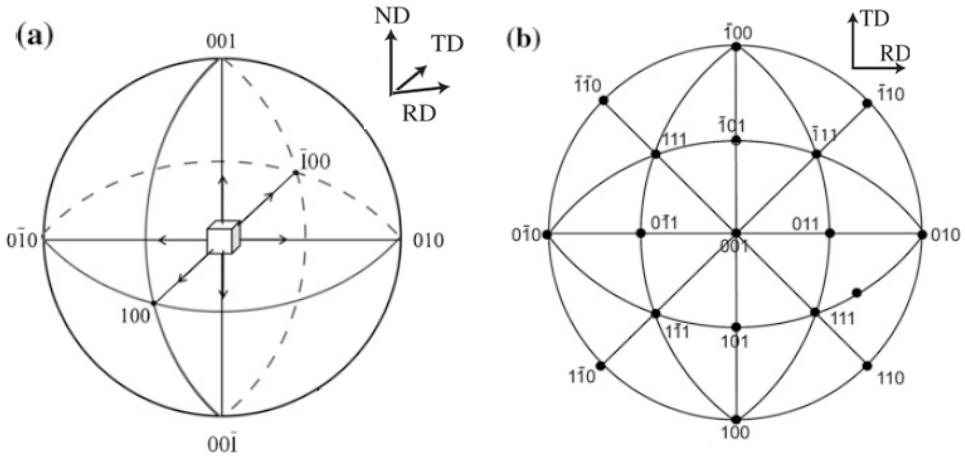


**Figure 8:** (a) Reference sphere and (b) stereographic projection with miller indices for crystallites with (001) aligned with the normal direction.

This provides a useful frame to compare pole figure data with known crystallographic directions. A sample with a different orientation facing the normal direction would of course

produce a different stereogram. For such a sample with its (001) face aligned in the ND, the (001) and (111) pole figures are shown over the full range of $0° \leq \alpha \leq 90°$ in Figure 8*.

(001) Pole Figure (111) Pole Figure

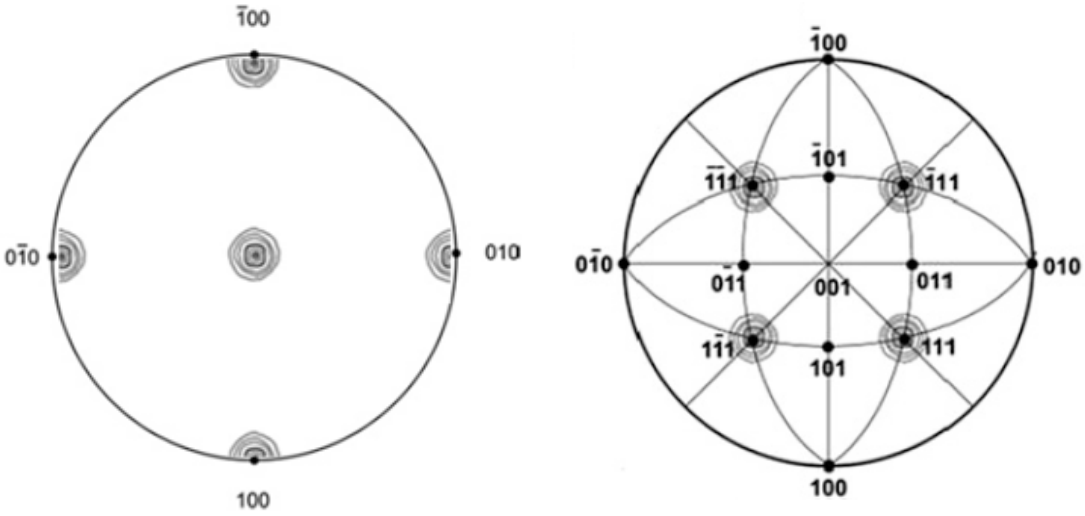


**Figure 9:** (001) (a) and (111) (b) pole figures on a single crystal sample.[12]

On the (001) pole figure we see diffraction peaks of all the equivalent {001} planes, and similarly in the (111) pole figure we observe all the {111} peaks. With the two pole figures, and the known crystal stereographs, we could deduce that the sample is approaching a single crystal.

Pole figures on polycrystalline materials show similarities to the single crystal cases, and may lie between entirely random and a perfect crystal. The pole figure on a perfectly random sample shows no distinct features at all with perfectly uniform intensity. The pole figure on a single crystal shows sharp, predictable diffraction peaks such as Figure 9. The polycrystalline case may show some combination of the two, where the crystallites are only aligned in one

direction. The same (001) and (111) pole figures for a polycrystalline sample with a <001> texture is shown in Figure 10.

A (001) scan would again show a strong center peak aligning with the normal direction at $\alpha = 0°$. The (111) scan looks very different however, and shows a ring positioned at $\alpha = 54.7°$, the known angle between the (001) and (111) planes in the cubic system. The angles between common Miller indices can be seen in table 1[2]. The four distinct (111) peaks in the single crystal case of figure 8* have smeared together into a ring. This can be understood as the crystallites having random in-plane orientations, although the (001) direction is still aligned with the ND. Similarly, one may also expect a ring to be found in the (001) measurement at $\alpha = 90°$ for the four distinct points on the rim (100, 010, $0\bar{1}0$, $\bar{1}00$) that are also be smeared around the stereograph.

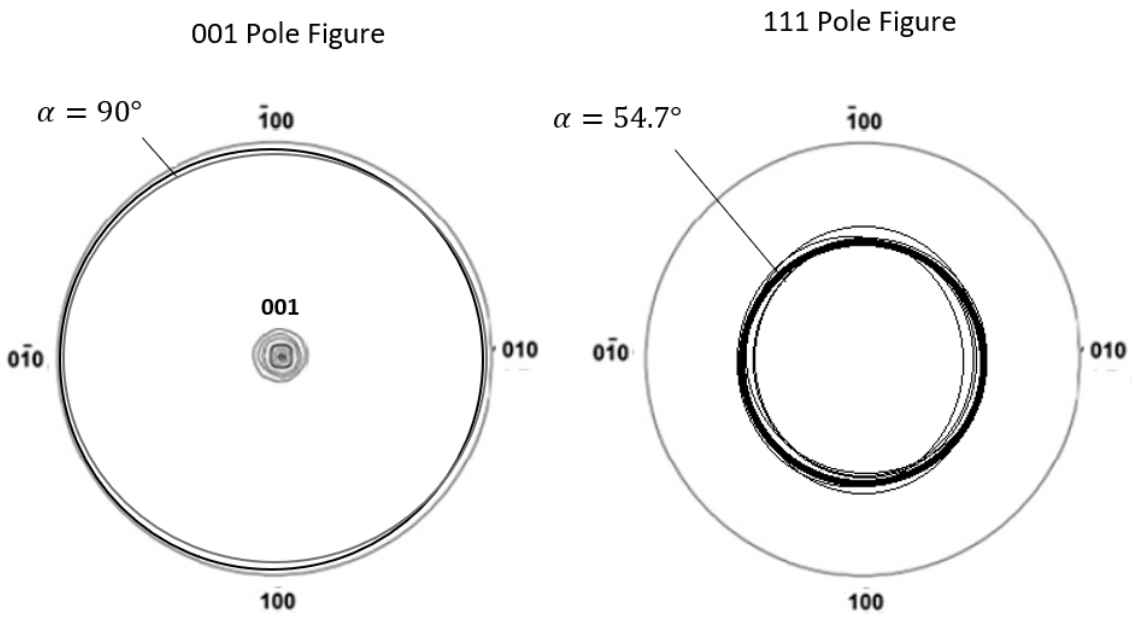


**Figure 10:** (111) and (001) Pole figures on a sample with <001> fiber texture.

When we collect x-ray data from a pole figure measurement, we are only be able to interrogate one $\boldsymbol{hkl}$ at a time. For this reason, it is well known that a single pole figure measurement cannot provide enough information to specify the orientation distribution. The pole figure represents a projection of the orientation space (where the $\phi_2$ coordinate is lost), and we cannot distinguish between crystallites rotated in-plane. Because of this, the accuracy of the ODF reconstruction is improved for each pole figure that can be measured.

| $h$ | $h'$ | $\angle(h, h')$ (°) |
|---|---|---|
| 100 | 100 | 0, 90 |
| | 110 | 45, 90 |
| | 111 | 54.7 |
| | 210 | 26.6, 63.4, 90 |
| 110 | 110 | 0, 60, 90 |
| | 111 | 35.3, 90 |
| | 210 | 18.4, 50.8, 71.6 |
| 111 | 111 | 0, 70.5 |
| | 210 | 39.2, 75 |
| 210 | 210 | 0, 36.9, 53.1, 66.4, 78.5, 90 |

**Table 1:** Angle between common miller indices. [2]

### 2.4.2 Interpretation of Inverse Pole Figures

One way to visualize the orientation distribution is through the inverse pole figure. The inverse pole figure shows the distribution of crystal planes $\boldsymbol{hkl}$ for a particular tilt, while the regular pole figure shows the distribution of tilts for a particular plane $\boldsymbol{hkl}$. When considering an inverse pole figure, we must specify the sample direction in which we are observing. The inverse pole figure is graphically represented by the same stereographic projection used in regular pole figures.

The Figures 10 (a) and (b) below show the full and truncated inverse pole figures in the normal direction ND for some material. This graph tells us that in the ND, the {011} set of planes is most prevalent in the normal direction. The units are the same as the ODF, in units of MRDs.

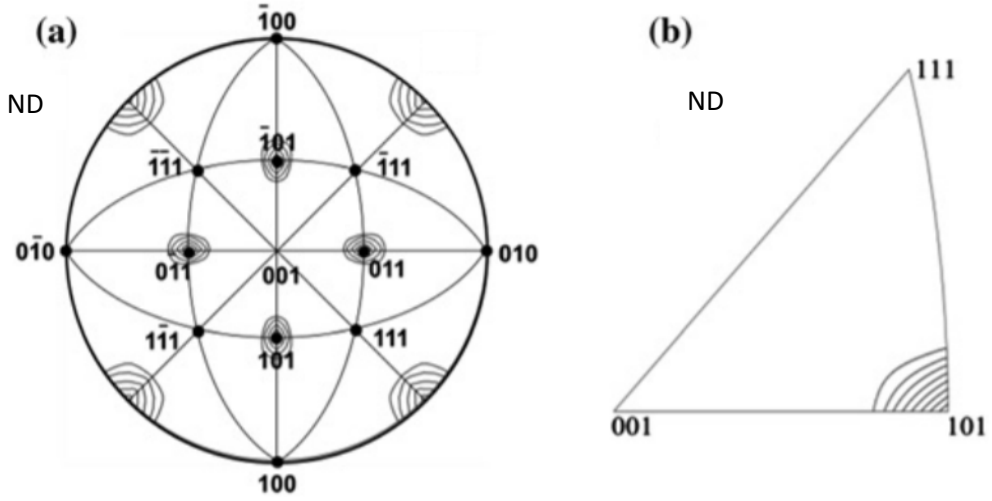


**Figure 11:** Full (a) and Truncated (b) inverse pole figures with <011> fiber texture.[12]

It is possible that an inverse pole figure such as that of Figure 11 could belong to either a polycrystalline sample with a strong fiber texture in the ND or a single crystal, and may be distinguished based on sharpness of the peaks and by additional inverse pole figures. For an ideal single crystal, we expect the inverse pole figure to show a single sharp peaks regardless of the direction we are looking at, and for their MRD value to diverge to infinity at the peak centers. A highly textured polycrystalline material would show peaks only in some directions, with much weaker peaks in its preferred directions. A perfectly random sample, by contrast, would never show peaks from any direction instead producing a uniform value with no contours for all crystal planes and for all directions. Figure 12 below shows inverse pole figures for 95% cold-rolled nickel as an example of how a polycrystalline material may appear. The contours are in units of MRDs.

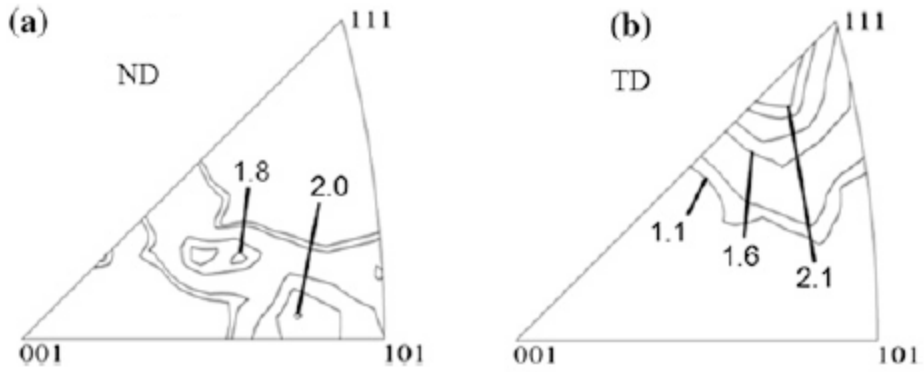


**Figure 12:** ND (a) TD (b) inverse pole figures of 95% cold-rolled nickel.[12]

The distribution of the crystal planes in the various directions, such as ND or TD can vary dramatically and depend strongly on the processing conditions. We may be able to infer from the Figure 10A that there are practically no (001) planes in either the ND or the TD.

The inverse pole figure can be considered a complete description of the ODF for a single direction (or fiber), and is more frequently used than the Cartesian orientation space due the large number of samples with a fiber texture. Due to its relation to the ODF, the inverse pole figure also has units of MRDs and can diverge towards 0 or infinity, where a value of 1 corresponds with a perfectly random sample.

In the stereographic projection for the cubic system there are 24 indistinguishable unit triangles. The inverse pole figure is truncated to a single triangle in part for convenience and to distinguish it visually from the pole figure. This truncated version may not be suitable for crystal systems with lower symmetries, but is employed overwhelmingly for cubic systems.

### 2.5 Calculation of the ODF

Calculation of the ODF from experimental data was an unsolved problem in the mid 20$^{th}$ century and its solution was fundamental in describing the properties of emerging powder and

polycrystalline materials. Independent methods were proposed by Bunge [7], Roe [9], and Williams [10,11]. There are two main methods for ODF construction from pole figure data: (i) fit the coefficients of the spherical harmonic functions to the pole figure data such as the technique used by Bunge and Roe, and (ii) discrete methods of calculating the ODF directly via an iterative process such as the least squares method by Williams[12].

Following from Bunge in the general case, the density of points distributed in orientation space can be represented by an orientation distribution function expressed in terms of the generalized spherical harmonics:

$$f(\phi_1, \Phi, \phi_2) = \sum_{l=0}^{\infty} \sum_{m=-l}^{+l} \sum_{n=-l}^{+l} C_l^{mn} P_l^{mn}(\Phi) e^{-im\phi_2} e^{-in\phi_1} \quad (6)$$

where $C_l^{mn}$ are coefficients, and $P_l^{mn}(\Phi)$ are the Legendre polynomials. Special forms of the function $P_l^{mn}(\Phi)$ may be employed for simplification in high symmetry systems, and Bunge does so frequently in the case of fiber textures or other special cases. The orientation distribution is completely described if the coefficients are known, so we must find a way to determine the coefficients from available pole figure data. It should be noted that an appropriate cut off value for $l$ must be specified that is sufficiently high enough to avoid truncation error.

To relate the pole figure to the orientation distribution, we start by considering that the pole figure is simply an integral of the ODF taken over the angle $\phi_2$. For a pole figure on the Bragg condition for the ***hkl*** set of planes, $P_{hkl}(\alpha, \beta)$, we can write:

$$P_{hkl}(\alpha, \beta) = \frac{1}{2\pi} \int_0^{2\pi} f(\phi_1, \Phi, \phi_2) d\phi_2 \quad (7)$$

This is the fundamental equation for the ODF computation where we transform from the pole figure coordinates $(\alpha, \beta)$ to the Euler angles $(\phi_1, \Phi, \phi_2)$. The method of solving this equation and finding the ODF from experimental data is known as the pole figure inversion [12].

In the series expansion method of Bunge and Roe, the pole figures are described in terms of a series expansion, whose coefficients can relate to the coefficients of the ODF:

$$P_{hkl}(\alpha, \beta) = \sum_{l=0}^{\infty} \sum_{m=-l}^{l} F_l^n(hkl) \quad K_l^n(\alpha, \beta) \tag{8}$$

where $F_l^n(hkl)$ are the coeffecients of the series expansion and $K_l^n(\alpha, \beta)$ is the spherical harmonic functions.

The coefficients of the pole figure expansion, $F_l^n(hkl)$, and the coefficients of the ODF expansion $C_l^{mn}$ can be related by the relationship:

$$F_l^n(hkl) = \frac{4\pi}{2l+1} \sum_{m=-l}^{l} C_l^{mn} K_l^{*m}(hkl) \tag{9}$$

where $K_l^{*m}(hkl)$ is the complex conjugate of $K_l^m$. This forms the system of equations that can be used to solve the coefficients $C_l^{mn}$ [13], and ultimately the ODF.

An index $J$ may be defined that describes the sharpness of the texture, where a value of 1 corresponds to a perectly random sample, and a value diverging to infinity corresponds to a prefect single crystal. The texture index J may be defined as:

$$J = \sum_{l,m,n} \frac{1}{2l+1} (C_l^{mn})^2 \tag{10}$$

The texture index is a single parameter that describes the sharpness of the texture, and has historically been used to provide a basis of comparison between textured materials. It provides a

quantitative measure of the preferred orientation without additional considerations for the details of the distribution, i.e., if the sample is <001> textured or <111> textured. The texture index only cares about the magnitude of the preferred orientation as compared to the entirely random case. The larger the coefficients $C_l^{mn}$, the greater the index.

### 2.6 Considerations for an X-ray Diffraction Intensities

The effects that determine the measured intensities in an x-ray diffraction experiment for polycrystalline films are dependent on the measurement geometry and the crystal structure. The principal elements are the effects of a non-coplanar geometry for values $\alpha \neq 0$ on the x-ray beam, and the properties of the crystal such as structure factor and symmetry group. After accounting for the other effects, we can make a statement as to the effect of the texture on the observed intensities. A quantitative analysis of x-ray intensities starts by considering the integral intensity of a diffraction peak in the $\theta/2\theta$ configuration. The integral intensity $I_{\boldsymbol{h}}^m$ with the reflection $\boldsymbol{h} = hkl$, can be written as:

$$I_h^m = SCF^m T_{\boldsymbol{h}} |F_{\boldsymbol{h}}|^2 m_{\boldsymbol{h}} Lp\, A_\alpha \tag{10}$$

Where $SCF^m$ is a generic instrumental scaling factor, $T_{\boldsymbol{h}}$ is the scaling factor due to texture, $F_{\boldsymbol{h}}$ is the structure factor, $m_{\boldsymbol{h}}$ is the multiplicity of a plane $\boldsymbol{h}$, $Lp$ is known as the Lorentz-polarization factor, and is the product of the Lorentz, geometry, and polarization factors. Lastly, $A_\alpha$ is the absorption factor for the pole figure configuration[2]. Lastly, we must also consider the background and defocusing corrections in the case for pole figure measurements. These factors will be addressed to give a thorough overview, however the factors comprising the Lorentz-polarization factor are typically not included in pole figure measurements. This is due to the fact that these factors scale all points within a pole figure for a given Bragg reflection by the same amount. For

the quantitative study of x-ray intensities, typically only an absorption factor and a defocusing factor (not listed in the equation above) are factored into the analysis. Also, a background subtraction is included.

### 2.6.1 Multiplicity

For polycrystalline samples, the intensities are scaled by their multiplicity due to crystal systems having multiple indistinguishable planes. Consider for example that the {111} set of planes has 8 indistinguishable planes $(111, \bar{1}11, 1\bar{1}1, 11\bar{1}, \bar{1}\bar{1}1, \bar{1}1\bar{1}, 1\bar{1}\bar{1}, \bar{1}\bar{1}\bar{1})$, while the {100} set of planes has only 6 $(100,010,001,\bar{1}00,0\bar{1}0,00\bar{1})$ . This causes a reflection to be overrepresented by the multiplicity of indistinguishable planes, and intensities must be scaled by their multiplicity when comparing reflections.

### 2.6.2 Lorentz-polarization Factor

The Lorentz-polarization factor is a product of Lorentz, geometry and polarization factors. By convention the term $Lp$ is used for the combination of these terms.

The geometry factor represents two effects on the spreading the Bragg peak over a circular segment of the focusing circle. In the $\theta/2\theta$ configuration, the intensities are spread over the Debeye rings and causes a dilution of the intensities by a factor $1/\sin 2\theta$. Secondly, the diffractomer measures an area region over a cone of scattered photons and intensity will scale with their density, $\cos\theta$. The geometry factor G in the $\theta/2\theta$ configuration is the product of these terms and can be given as $G = 1/2 \sin\theta$ [13] .

In the pole figure configuration, the geometry factor is given as [2]:

$$k(\omega, \delta) = \frac{1}{\sin(\omega+\delta)} + \frac{1}{\sin[2\theta_0-(\omega+\delta)]} \tag{11}$$

where $\omega$ is the sample tilt, and $\delta$ is the divergence of the beam path.

The polarization factor $\bar{C}^2$ arises due to the fact that x-ray emissions from an x-ray tube have random polarizations. The interactions of these photons can be shown to be shown to scale the intensities by the factor:

$$\bar{C}^2 = 1 + \frac{\cos^2 2\theta}{2} \tag{12}$$

Lastly, the Lorentz factor is a measure of the time of reflection permitted to each reflection[14]. The term L is commonly given the value:

$$L = 1/\sin 2\theta \tag{13}$$

### 2.6.3 Absorption Factor

One effect of a non-coplanar geometry on the intensities arises from the change in path length through the sample surface. As the sample is tilted through angles $\alpha$, the total path length in the sample is changed. The total path length $2l$ can be shown to be equal to $2z/sin\theta cos\alpha$ where $z$ is the depth coordinate[2]. Integrating the intensities from thickness of the film $t$, we can yield:

$$A_\alpha = \left[1 - \exp\left(-\frac{2\mu t}{sin\theta \cos\alpha}\right)\right] \tag{14}$$

As an appropriate absorption factor.

### 2.6.4 Defocusing Factor

A second major consequence of the non-coplanar geometry is the broadening of the x-ray footprint on the sample surface as seen in Figure 13. This is considered the defocusing effect, and can become quite severe for large angles of $\alpha$.

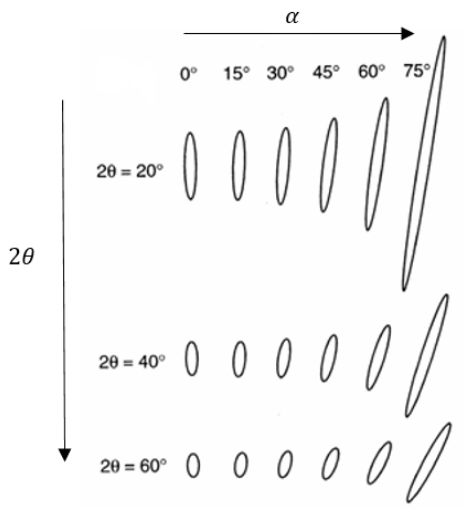


**Figure 13:** Change in shape and orientation of irradiated footprint on sample surface for tilts $\alpha$ and Bragg angle $2\theta$.[14]

The defocusing effect reveals itself in the diffractogram as a broadening of the peaks because the cone of diffracted intensities broadens. To obtain a correct interpretation of the effect, a randomly oriented powder sample must be used as a reference. If an appropriate sample is not available, the pole figure measurement can be limited to lower values of $\alpha$ from the full range. In parallel beam configuration, values of 85° – 89° may be achieved, while Bragg-Brentano configurations may need to be limited to as low as $\alpha = 70°$ [2]. The defocusing effect must also be obtained for each plane $\boldsymbol{hkl}$ that pole figure measurements are to be taken. While the effect is purely geometric and can be calculated, in practice it has been obtained experimentally as seen in Figure 14. The pole figure data for the sample is then corrected for the defocusing effect by dividing by the fractional intensity $\frac{I}{I_0}$ for each point in $\alpha$.

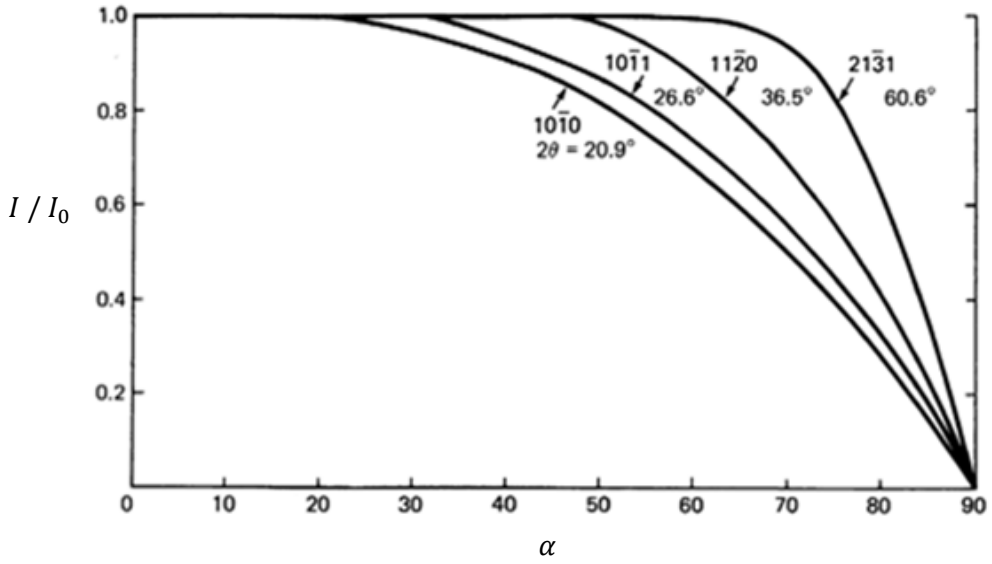


**Figure 14:** Intensity correction for x-ray pole figure measurements on quartz in the Bragg Brentano configuration. [14]

### 2.6.5 Background Subtraction

The background intensities during pole figures must also be accounted for and removed. The background correction can be performed by scanning from $\alpha = 0°$ to 90° with a 3° variation $\theta/2\theta$ angle. This is typically performed by measuring over the $\chi$ axis in the diffractometer. The measurement can be taken at a high value, $2\theta + 3°$, and a low value, $2\theta - 3°$. For each value $\chi$, an average of the high and low measurements values are averaged and subtracted from the nominal $2\theta$ values. A full pole figure to measure the background is generally unnecessary, and would only be required if the sample does not have symmetry through $\beta$. Figure 15 shows the general process, where an average of the high and low background measurements, $B_h$ and $B_l$, are taken.

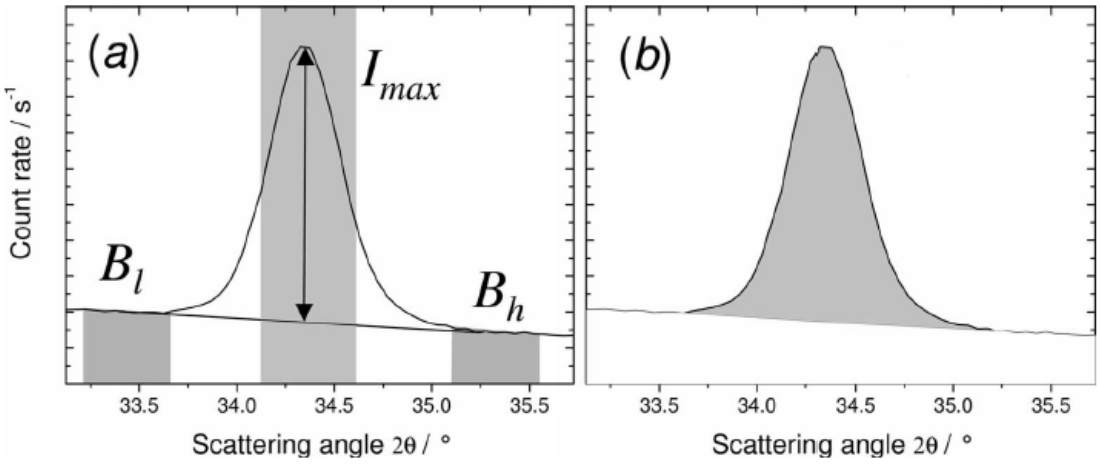


**Figure 15:** Linear background correction for a pole figure.[2]

### 2.6.6 Substrate Peak Removal

In pole figure measurements, a particular Bragg condition is selected and the diffractometer cannot distinguish diffracted intensities from different materials. This may be problematic if the materials have neighboring peaks in the $\theta/2\theta$ coordinate, as they will certainly interfere with each other. The subtraction of the non-representative intensities may take on different methods depending on the materials in question (single crystal, polycrystalline, multilayers). Substrate peak removal is considered here due to its applications for CVD diamond on silicon.

Figure 16 shows an image of raw pole figure data taken from the 1.5% sample. You can see in both scans a few distinct points that dominate the intensity of the graphs. These are underlying silicon peaks. In the (220) pole figure for example, the 8 fold symmetry seen is from the {331} planes of silicon. Data points in the top graph can be higher than 1000 counts, however anything above this threshold is color-coded the same.

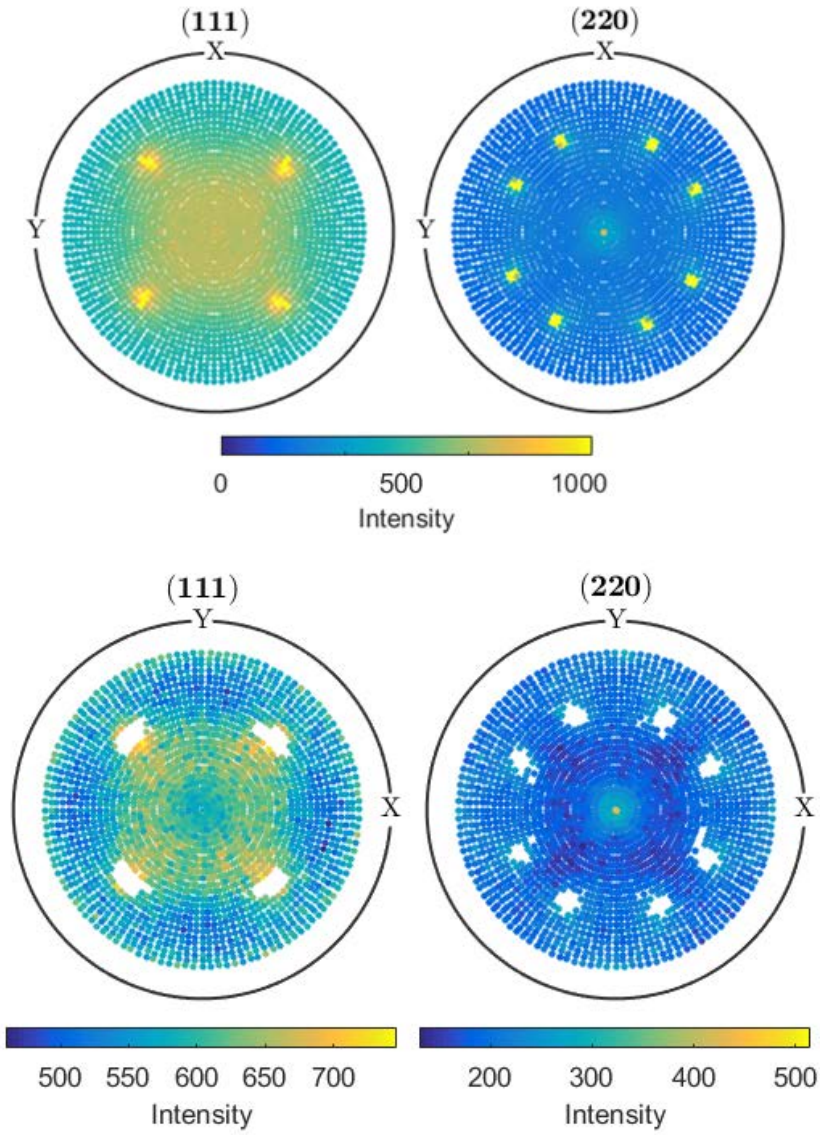


**Figure 16:** Pole figure measurements before (top) and after (bottom) outlier of Group I 1.5% methane sample.

Although the silicon peaks are quite sharp, their intensities are very large compared to the polycrystalline diamond and can affect data points in the proximity. The diamond peaks, depending on the film, have an intensity on the order of 500 to 5000 counts depending on thickness and growth

conditions. The silicon peaks can exhibit intensities on the order of 100,000 and can exhibit a few hundred to a few thousand counts for values between 3 and 6 degrees of the silicon peak.

The subject of substrate peak removal is not discussed in literature for pole figures specifically, so general outlier removal is proposed here. Substrate peaks were removed by the combination of two outlier removals. First a standard deviation, $\sigma_{\alpha_i}$, is calculated for all data points with equal $\alpha$, and data points 3 standard deviations above the median, $Md_{\alpha_i}$, value are subtracted. The subscript alpha is intended to show that the group has equal $\alpha$ values, and the subscript $i$ is intended to indicate which alpha value. A second outlier removal proceeds by recalculating these standard deviations and median values. Rings comprised of varying $\beta$ points with a shared value $\alpha$ far from silicon peaks were found to have a normal distribution, where the mean values of the distributions were nearly identical to the median. The ratio of the standard deviations to the median values, $\sigma_{\alpha_i} / Md_{\alpha_i}$ were calculated for all intensity rings. This ratio was similar for all points far from the silicon peaks and corresponds to the signal to noise ratio. The median value of all these ratios, $\sigma_{\alpha_1} / Md_{\alpha_1}$, $\sigma_{\alpha_2} / Md_{\alpha_2}$ … , was taken. Data points were removed if they fell above a value equal to the median for each ring, $Md_{\alpha_i}$, plus the median $Md_{\alpha_i}$ times the median of the ratios times 1.6. The value of 1.6 is chosen due to its correspondence with a confidence interval of 90%, and was found to generally produce a reasonable threshold across the data sets.

To provide clarity, an overview of the data processing is given below in Figure 17. First, data points affected by underlying silicon peaks are removed. The data points then undergo a background subtraction, and finally they are scaled according the absorption factor in the pole figure configuration.

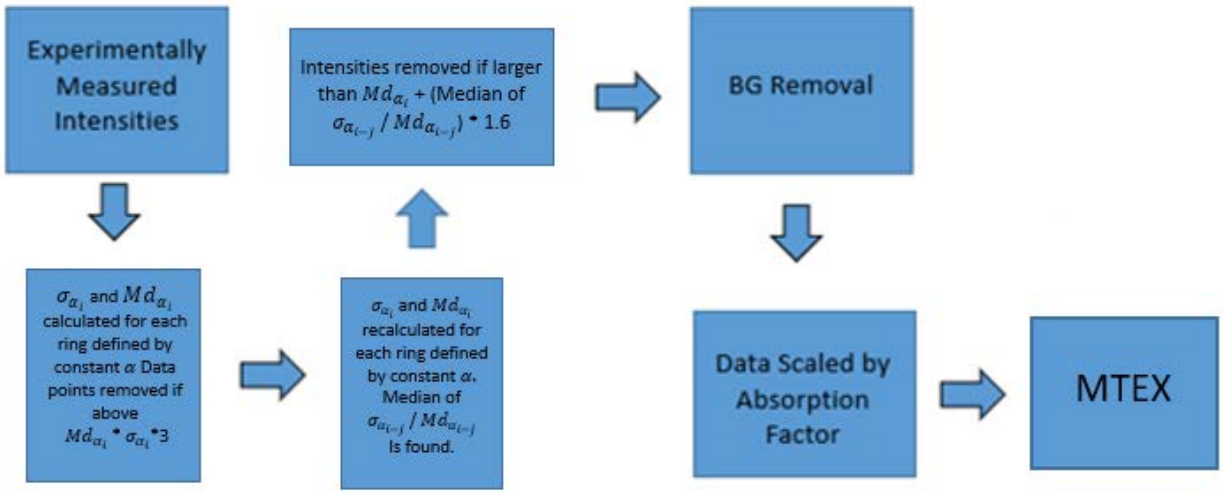


**Figure 17:** Flow chart for corrections to measured intensities.

### 2.7 Texture in CVD Diamond

Texture formation in CVD Diamond can be understood through the van der Drift evolutionary selection model [15,16] as seen in Figure 18. The crystallographic direction with the highest growth rate in the substrate normal direction will be favorable, leading to a strong fiber texture in the sample normal direction. The grains that grow the fastest vertically overtake smaller grains, and dominate the orientation of the film. [16]

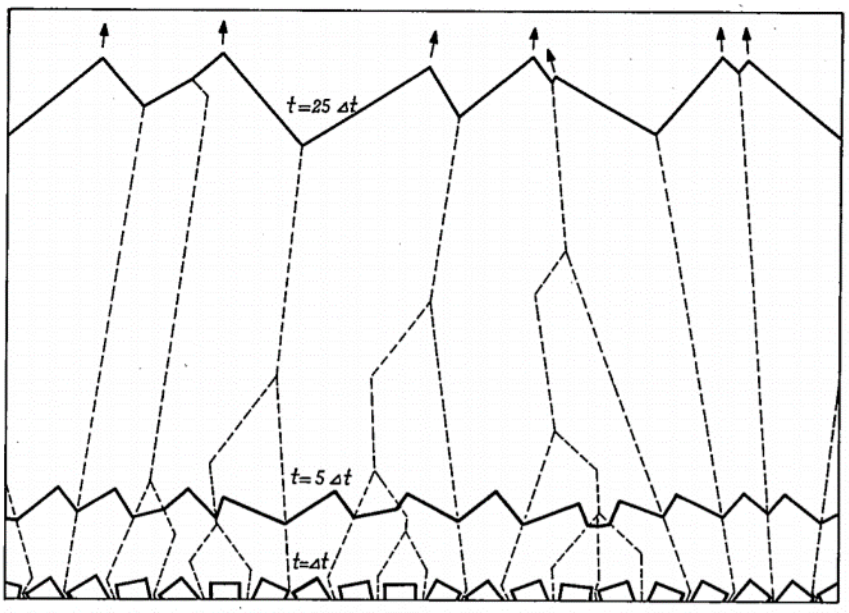


**Figure 18:** van der Drift growth model showing crystallite formation over time.[18].

Growth rates along the various growth directions is a kinetics driven process, and depends on the surface energy, multiplicity of the growth plane, and on the deposition parameters[18]. The addition of new carbon atoms to a crystallite is in part governed by the number of available nucleation sites and the availability of the various methane radicals.

The growth mechanism on the {111} and {100} surfaces has been investigated considerably in the literature. In the texture analysis carried out by Liu et. at (2009) [15] using a DC arc jet technique, they analyzed their work in the context that deposition along {111} planes occurs via an interaction of radicals with at least one free bond ($CH_3$, $CH_2$, $CH$, $C$) and one radical with at least three ($CH_1$ or $C$). Further, that growth along the {100} direction proceeds with two $CH_2$ bonds. This follows from the models by Goodwin and Butler [19] on CVD diamond growth and the {111} growth mechanism suggested by Tsuda et al. [20].

The occurrence of twins and microtwins during growth has also been shown to affect the texture of the film through destabilization of growth [15,16], and was the subject of the growth model suggested by Meakin[21] for the rapid formation of <110> textures seen in many films. For the

diamond structure, twinning planes can occur along the directions <111> and <110> with the first being more common[15]. These twinning events reorient the crystal frame, and a summary of the transformations can be seen in Table 2. There are more rotations that lead <111> and <110> into an equivalent direction than there are for the <100> directions, which may cause deterioration of the <100> faces in hot-filament growth [22].

| Twinning | Rotation angle/axis | Change of lattice plane after primary and secondary twinning |
|---|---|---|
| Primary (Σ3) | 60°/⟨111⟩ | {001} — {221} (1st) — {148}, {447}, or {001} (2nd) |
| | | {110} — {110} or {114} (1st) — {110}, {114}, {778}, or {4,5,11} (2nd) |
| | | {111} — {111} or {115} (1st) — {111}, {115}, {11,11,1}, or {5,7,13} (2nd) |
| Secondary (Σ9) | 38.9°/⟨110⟩ | {001} — {447} or {148} |
| | | {110} — {110}, {114}, {778}, or {4,5,11} |
| | | {111} — {115}, {5,7,13}, or {11,11,1} |

**Table 2:** Possible transformations by primary and secondary twinning in diamond [15].

For CVD diamond grown by hot filament, films showing a variety of textures including <111>, <001> and <110> have been reported[22], although the exact deposition parameters are generally guarded. They reported that <111> and "cauliflower" <110> textured films suffer from a high densities of twinning, where <100> films are much more stable to defects.

Increased substrate temperature has been linked with enhancement of the <001> texture fiber and has been reported for hot filament[23] and DC arc methods[15]. The methane decomposition and diamond deposition rates increase with rising substrate temperatures [24,25], and it is expected that the generally elevated consumption rate of $CH_2$ limits the availability of $CH$ for {111} growth[26]. Additionally, the increased substrate temperature is expected to cause hydrogen on the growth front to be more easily extracted by the hydrogen in the gas phase leading to more nucleation sites and a reduction of stacking faults and twins [27,28].

Elevated methane concentrations and film thickness have been associated with the <110> texture. Liu et. at [15] propose that increased methane concentrations lead to increased consumption

of $CH_2$ radicals, again limiting the availability of $CH$ radicals. Increased thicknesses are predicted to favor the fastest growing direction according to the van der Drift model, which tends to be <110>.

### 2.8 MTEX

Two general classifications are used for the estimation of an ODF: direct and indirect. [33] There is some inconsistency regarding the terminology of methods, but for our purposes, we will adopt this language. Direct methods use a series of measurements of complete orientation information such as electron backscatter diffraction. Indirect methods make up the majority of methods for ODF calculation and rely on pole figure measurements as an input. These methods compare the ODF through the pole figure inversion equation, and attempt to minimize the error between the two [33]. The values of the initially estimated ODF are then continuously improved to fit the associated measured pole figure values [12].

Important indirect methods include, but are not limited to the WIMV method [29,30], the vector method [31,32], and the component method [33]. These methods and their implementation in software code only consider the orientation distribution function at discrete locations in the orientation space, which can limit the step size of the measurement or may force binning of the measurement intensities to fit a regular grid [30,34]. This is because these methods do not consider a continuous function, but rather they take a truncated version of the series expansion. As such, these methods are sometimes referred to as discrete methods. Furthermore, its been shown that these methods do not computationally apply to sharp textures [36].

The MTEX algorithm, a freely available MatLab™ based toolbox, is a recently developed indirect method that provides a way to represent, analyze and interpret crystallographic textures from x-ray pole figures and electron backscatter diffraction measurements. The MTEX algorithm employs a unique algorithm for the calculation of the ODF and offers some key advantages over the other methods.

First, MTEX allows for arbitrarily step sizes in measured diffraction intensities, which is key to enabling area detectors for the use of quantitative texture analysis. Secondly, the algorithm has been shown to better approximate sharp textures than other methods [36], and can keep the harmonic degree relatively large (up to about 500) reducing errors associated with truncation.

The unique algorithm that MTEX employs is based on the recognition of the relationship between a known integral operator, the Radon transformation, and the general axis distribution function. Let $K_s = \{x, y, z\}$ be a right handed coordinate system for the sample, and let $K_C = \{a, b, c\}$ be a right-handed coordinate system for the crystal. A rotation **g** is the orientation of the crystal if it rotates the sample coordinate system to the crystal coordinate system by $\boldsymbol{g}x = \boldsymbol{a}, \boldsymbol{g}y = \boldsymbol{b}, \boldsymbol{g}z = \boldsymbol{c}$. Additionally, let $\boldsymbol{r} = (\boldsymbol{u}, \boldsymbol{v}, \boldsymbol{w})^T$ be a coordinate vector with respect to the sample coordinate system, and let $\boldsymbol{h} = (\boldsymbol{h}, \boldsymbol{k}, \boldsymbol{l})^T$ be a corresponding coordinate vector with respect to the crystal coordinate system that has the same direction.

The axis distribution function (Bunge, 1982) or the pole density function (PDF) (Matthies et al., 1987), is the pole figure function of equation (7) over a general range. It can be considered by integrating the function $f(g)$ over all orientations where the crystal directions $\boldsymbol{h}$ are parallel to the sample direction $\boldsymbol{r}$.

$$P(\boldsymbol{h}, \boldsymbol{r}) = \frac{1}{2\pi} \int_{h \,||\, r} f(g) dg \tag{15}$$

On an important side note, Bunge addresses that the function $P(\boldsymbol{h}, \boldsymbol{r})$ cannot distinguish between $+\boldsymbol{h}$ and $-\boldsymbol{h}$, a fundamental issue when trying to solve for the ODF that causes the function $f(g)$ to only contain even exponents in the series expansion. This is known as the ghost error, and different methods for obtaining corrected ODFs include the zero-range method [37,38], the quadratic method [39], the positivity method [40], the "maximum entropy method" and the method proposed by Lücke et. al [41,42].

It's shown that the inversion of the pole figure to the ODF can be recognized as the Radon transformation $\mathcal{R}$, a historically known integral transform, as it acts on a function $f(h,r)$. It can be written

$$\mathcal{R}f(h,r) = \frac{1}{2\pi}\int_{h\,||r} f(g)dg \tag{16}$$

The transformation $\mathcal{R}$ is an integral transform which takes a function $f$ defined on a plane to a function $\mathcal{R}f$ defined on the space of lines in the plane, whose value at a particular line is equal to the line integral of the function $f$ over the line. The relationship between an ODF $f$ and its Radon transform $\mathcal{R}f$ is one to one, whereas the relationship between the pole density function $P$ and the ODF is not, which offers some advantages in its computation.

A model is assumed that the true ODF can be expanded into a linear combination of radially symmetric basis functions, a well known technique in approximation theory on the sphere and other manifolds [36]. A family of these functions are formed by the de la Vallée kernel, and offer computational advantages when working with the Radon transformation.

To summarize the MTEX algorithm, MTEX fundamentally operates by proposing an ODF that is comprised of up to 100,000 simple bell shaped distributions. These distributions are formed by the de la Vallée kernals, a set of distribution functions that are themselves formed by a set of Fourier coefficients. The diffraction intensities are modeled into a pole density function (PDF) with appropriate crystal symmetries by assuming the intensities have a Poison distribution, and that the intensities correspond to the mean value of the Poison distribution. The Radon transformation of the proposed ODF is then compared to the PDF using a weighted least squares estimator. This least squares estimator is weighted in the sense that deviations from small diffraction intensities are more severely penalized than deviations from large diffraction intensities, or more precisely that the least-squares functionals are weighted with the inverse expected variance of the measurement error [36]. The least squares estimator is itself a minimization problem, which is solved using a modified

steepest decent algorithm (Kim, 2002, Bardsley & Nagy, 2005). A flow of the MTEX process is shown in Figure 19, although this does not necessarily indicate the order of operations in the software code.

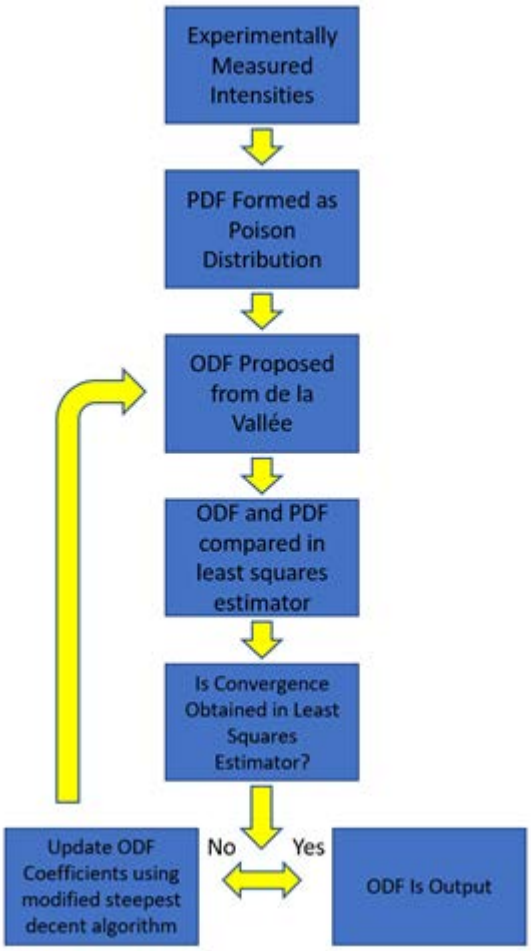


**Figure 19:** Basic flow chart for MTEX algorithm. [18].

For a full explanation of the MTEX approach, readers are referred to [35,36] Estimates for the accuracy of texture measurements have not been widely used, although some attempts to explore uncertainties in the pole figures have been undertaken [33]. A variety of sources of uncertainty have been investigated for an estimated ODF including errors in the pole figure

measurement [43,44], truncation error in the series expansion method [36], limitations in the number of available pole figures[7], and differences between ODF solving techniques and their software [45].

# III. EXPERIMENT

Diamond films were grown using the Hot Filament CVD method using methane, hydrogen, oxygen and argon gasses. Samples were prepared using a (100) oriented silicon wafers and a novel photoresist diamond seeding method that produces nucleation density of approximately $10^{10} cm^{-2}$. Group I samples were grown at 1.50%, 2.25%, 3.0%, 3.75% and 4.5% $CH_4/H_2$ ratios for 8 hours. Group II samples were grown to a target thickness of 1.2 $\mu$m, with $CH_4/H_2$ ratios of 1.5%, 3%, and 4.5%. The gas flow rates were 2 lpm $H_2$, 3 sccm $O_2$, with varying methane concentrations. The 1.5% $CH_4/H_2$ from Group II incidentally had an 8-hour growth, and is also the 1.50% sample in Group I. All samples were grown using a pressure of approximately 20.8 torr, and a 6mm sample to wire distance with a substrate temperature of 670°F as measured by an IR pyrometer.

Pole figures for the texture analysis of the films was measured by a Rigaku SmartLab X-ray Diffractometer, using a 2mm x 2mm spot size, a parallel beam configuration, no Soller slit or collimator, and an open detector. The spot size was chosen as a compromise between intensity and selection area, considering that measurements were taken 15mm apart. PB was selected to improve defocusing errors. An open detector configuration was selected as it is well known that pole figures should be scanned with an open detector. Data was collected at 3° intervals in both $\alpha$ and $\beta$, with an integration time of 1 second. The scanning range was limited to $\alpha = 70°$, due to the lack of an appropriate powder sample for a defocusing correction. Measurements were taken at diamond's (111), (220) and (311) diffraction peaks at 43.93°, 78.93° and 93.83° degrees respectfully, although the (311) pole figures were excluded from analysis due to the propagation of underlying silicon peaks. A variation in grain size had been found for these samples corresponding with the radial distance from the center of the wafer, so additional pole figures were taken at 10mm intervals from the center starting at 15mm to investigate the effect of grain size on the texture. The samples

were only aligned once at the 15mm positions. In hindsight this may cause issues for proceeding measurements as diamond films can exhibit high stresses and may bow the substrate wafer.

Estimation of the ODF was performed using the MTEX toolbox. The inverse pole figures and the texture index were found using MTEX. Intensities were first corrected for outliers, then a linear background subtraction was performed. Intensities were then scaled according to the absorption factor in the pole figure configuration. A defocusing factor is not applied.

The grain size was measured using the Heyn Linear Intercept method [46] from SEM images, using lines that produced at least 50 intersections. SEM images were measured on a Helios Nanolab 400 FIE SEM at 10kV and .34 nA Film thickness was measured using a Bruker DektakXT profilometer.

# IV. RESULTS

*Orientation Distribution*

*Group I*

The strength of the texture, as indicated by the texture index $J$, was found to be most dependent on increased thickness, though only the 4.50% methane sample showed a noticeable increase. The Group II samples, with relatively low thicknesses, showed a texture index associated with a nearly random distribution. The results of the texture index, thickness and grain size for the Group I samples is summarized below in tables 3. The inverse pole figures of Figure 18 show a growing trend towards a <220> fiber texture with increased methane concentrations, shifting from a <111> texture in the 1.5% sample, to a clear <220> texture in the 2.25% sample and above. The increased texture index with increasing thickness is predicted according to the Van der Drift growth model

| Position | | Group I – 8 Hours | | | | |
|---|---|---|---|---|---|---|
| | $CH_4/H_2$ | 1.50% | 2.25% | 3.00% | 3.75% | 4.50% |
| 15mm | $J$<br>Thickness (um)<br>Grain Size (um) | 1.012<br>1.15 ± .06<br>.68 ± .04 | 1.023<br>2.14 ± .05<br>.86 ± .06 | 1.020<br>4.21 ± .08<br>1.20 ± .09 | 1.084<br>7.40 ± .11 | 1.762<br>12.77 ± .13 |
| 25mm | $J$<br>Thickness (um)<br>Grain Size (um) | 1.004<br>1.12 ± .05<br>.61 ± .03 | 1.063<br>2.09 ± .05<br>.87 ± .06 | 1.024<br>4.20 ± .09<br>1.18 ± .10 | 1.075<br>7.27 ± .10<br>. | 1.797<br>12.01 ± .13 |
| 35mm | $J$<br>Thickness (um)<br>Grain Size (um) | 1.005<br>1.08 ± .05<br>.57 ± .03 | 1.061<br>2.08 ± .05<br>.85 ± .05 | 1.046<br>4.18 ± .09<br>1.19 ± .10 | 1.074<br>7.24 ± .11 | 1.746<br>11.20 ± .12 |

**Table 3:** Summary of the texture index $J$, thickness, and grain size by sample and measured position for Group I.

(a)

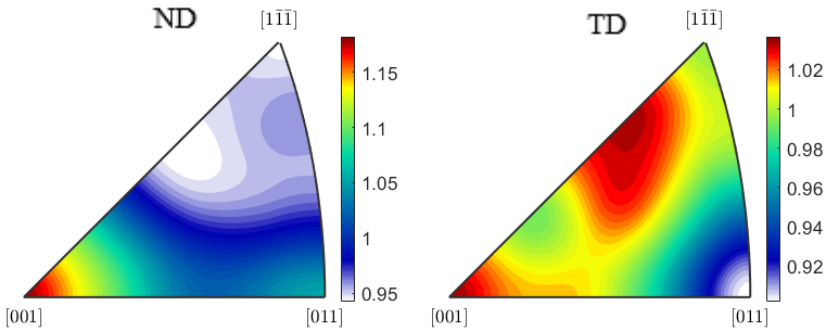
ND
[1$\bar{1}\bar{1}$]
1.15
1.1
1.05
1
0.95
[001]
[011]
TD
[1$\bar{1}\bar{1}$]
1.02
1
0.98
0.96
0.94
0.92
[001]
[011]

(b)

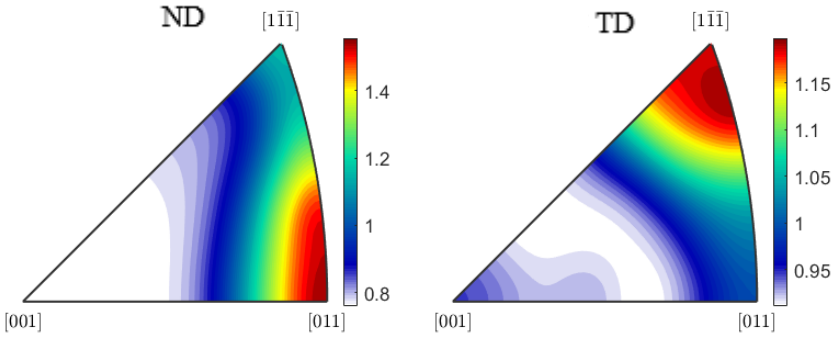
ND
[1$\bar{1}\bar{1}$]
1.4
1.2
1
0.8
[001]
[011]
TD
[1$\bar{1}\bar{1}$]
1.15
1.1
1.05
1
0.95
[001]
[011]

(c)

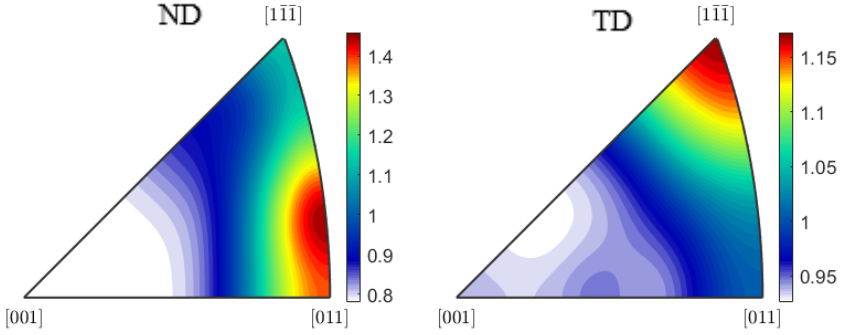
ND
[1$\bar{1}\bar{1}$]
1.4
1.3
1.2
1.1
1
0.9
0.8
[001]
[011]
TD
[1$\bar{1}\bar{1}$]
1.15
1.1
1.05
1
0.95
[001]
[011]

(d)

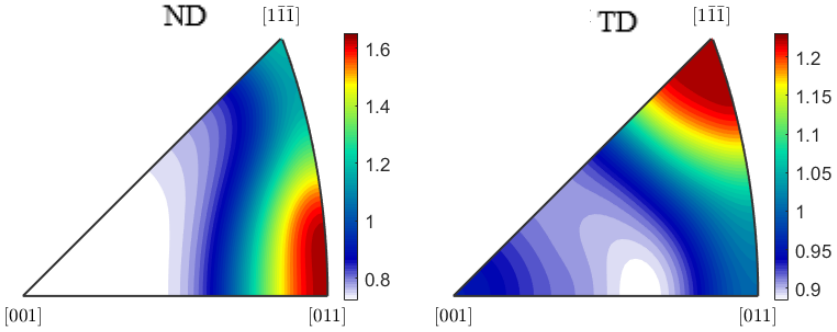
ND
[1$\bar{1}\bar{1}$]
1.6
1.4
1.2
1
0.8
[001]
[011]
TD
[1$\bar{1}\bar{1}$]
1.2
1.15
1.1
1.05
1
0.95
0.9
[001]
[011]

(e)

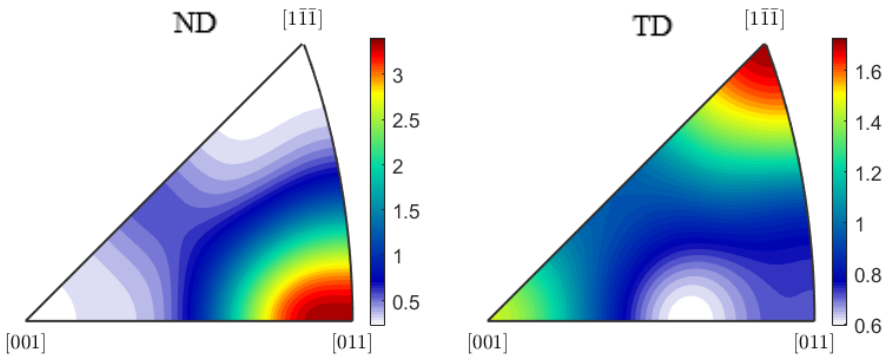


**Figure 20:** Inverse pole figures of at (a) 1.5%, (b) 2.25% (c) 3.0% (d) 3.75% and (e) 4.50% $CH_4/H_2$ samples of Group I (8 hours) at 25mm.

*Group II*

The texture index, thickness, and grain size of the Group II samples are summarized below in table 4. The inverse pole figures for these samples are also reported.

| Position | | Group II – 1.2 um Target Thickness | | |
|---|---|---|---|---|
| | $CH_4/H_2$ | 1.50% | 3.00% | 4.50% |
| 15mm | $J$<br>Thickness (um)<br>Grain Size (um) | 1.012<br>1.15 ± .06<br>.68 ± .04 | 1.018<br>1.32 ± .05<br>.74 ± .06 | 1.010<br>1.17 ± .05<br>.63 ± .07 |
| 25mm | $J$<br>Thickness (um)<br>Grain Size (um) | 1.004<br>1.12 ± .05<br>.61 ± .03 | 1.018<br>1.29 ± .05<br>.67 ± .05 | 1.009<br>1.14 ± .06<br>.60 ± .07 |
| 35mm | $J$<br>Thickness (um)<br>Grain Size (um) | 1.005<br>1.08 ± .05<br>.57 ± .03 | 1.019<br>1.27 ± .05<br>.65 ± .05 | 1.012<br>1.14 ± .06<br>.57 ± .06 |

**Table 4:** Summary of the texture index $J$, thickness, and grain size by sample and measured position for Group II.

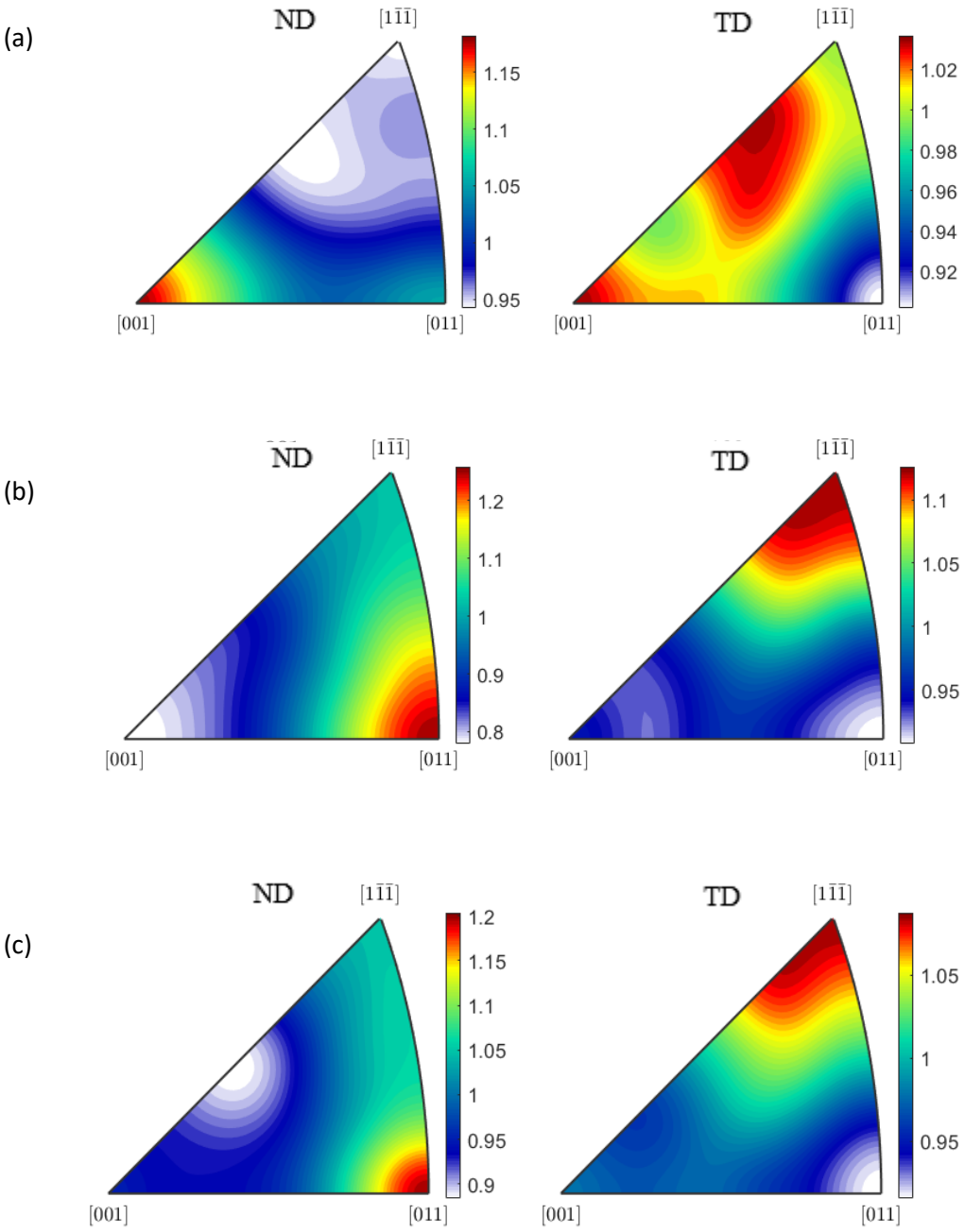


**Figure 21:** Inverse pole figures of at (a) 1.5%, (b) 3.00% (c) 4.50% $CH_4/H_2$ samples of Group II (1.2 um target thickness) at 25mm.

The <220> texture for higher methane concentrations may be explained in literature by the elevated growth rate, and by relation, elevated consumption rate of $CH_2$. The elevated consumption of $CH_2$ limits further acquisition of $CH$ for growth on the {111} surface [26], causing a reduction of {111} growth and a relative balance of (111) and (001) growth rates, leading to a <110> texture.

*Morphology*

The orientation distribution may also be effected by the increased propensity of twinning as can be observed visually by SEM. Figure 16 (a-c) shows SEM micrographs of $CH_4/H_2$ ratios 1.5%, 3%, and 4.5% taken at 15mm from the center of the wafer. The morphology of the films show that the 1.5% methane sample had octahedron features with large (111) faces, with a twinning destabilization of the (100) faces leading to the appearance of the commonly seen "5-fold" symmetry. Increasing the methane concentration led to higher deposition rates, but an increasing tendency for twining and the emergence of the "cauliflower" structure seen in the thick 4.5% sample Figure 16(d). The cauliflower morphology is known to be associated with a high defect and twinning density [23]. Interestingly, the 4.5% sample initially is shown to originally have defined grains, giving way to the cauliflower texture as the deposition times increases. As discussed here in section 2.7, the <110> texture may be enhanced by the increased number of twinning events.

The effects of twinning on the morphology can be visualized in Figure 17. Free standing grains for (a) 1.5%, (b) 3% and (c) 8 hour 4.5% $CH_4/H_2$ can be seen. It's clear that as the methane concentration increases, the propensity for twinning is increased. This has the effect of reducing the size of the crystal domains and reducing the long-range order of the crystallite.

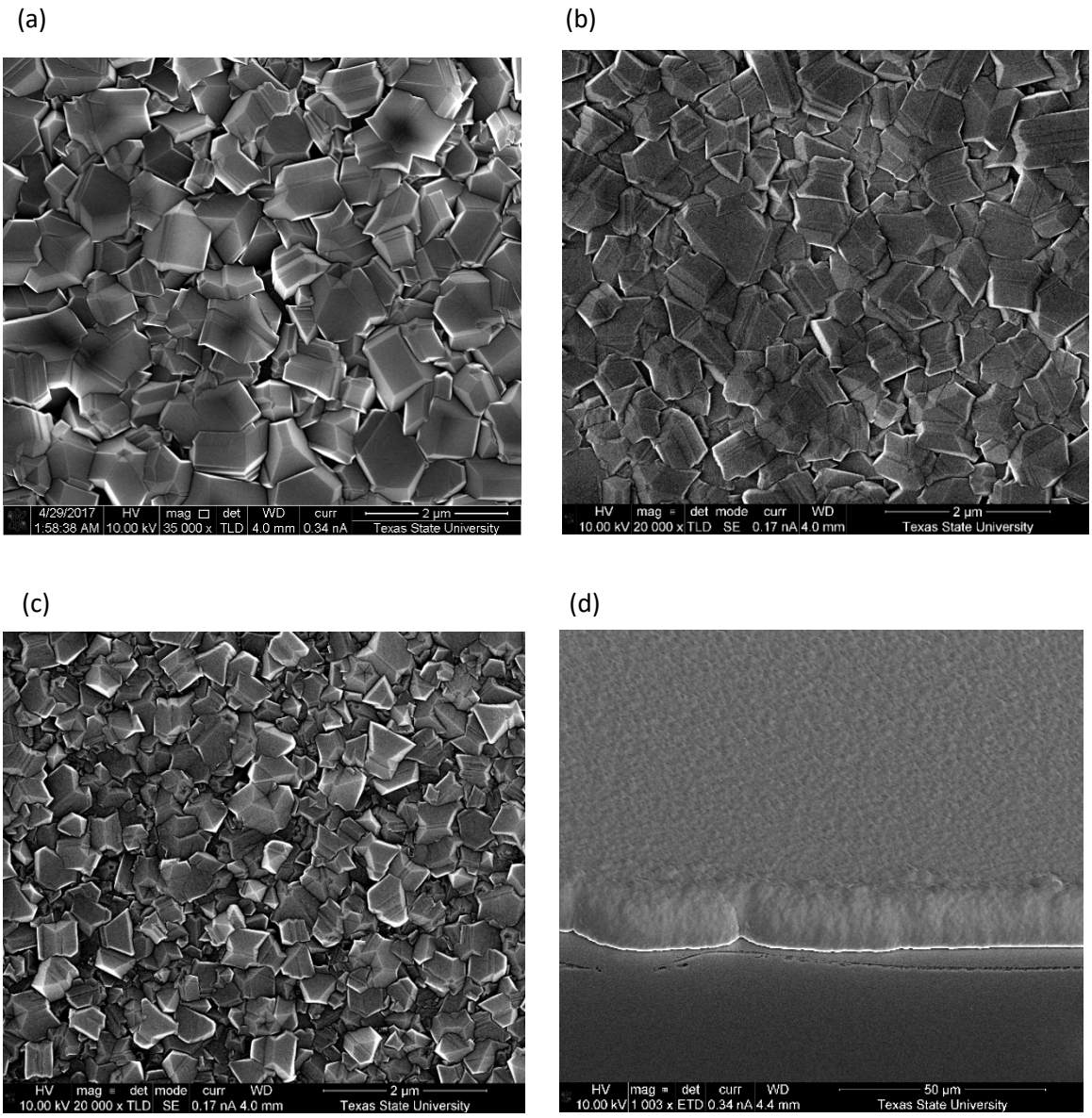


**Figure 22:** SEM Micrographs of Group II CVD Diamond samples 15mm from center at (a) 1.5%, (b) 3% (c) 4.5% $CH_4/H_2$, and (d) 4.5% 8h $CH_4/H_2$ from Group I.

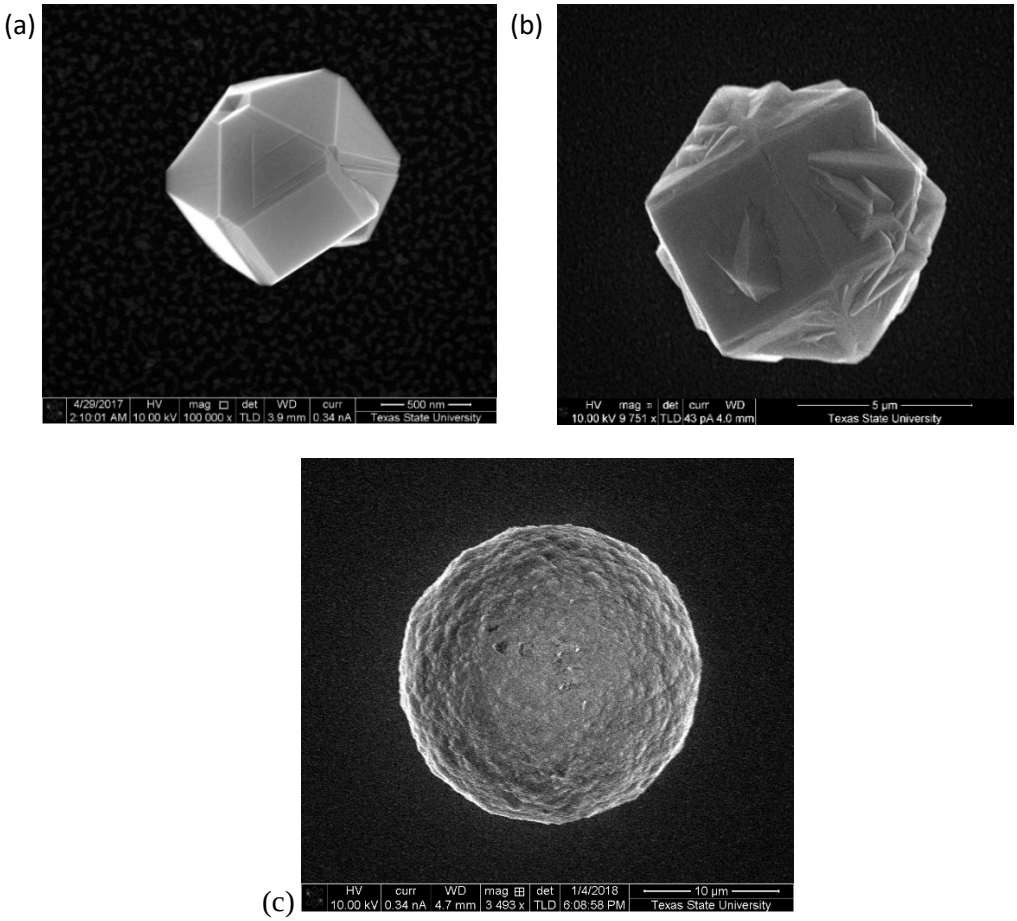


**Figure 23:** SEM Micrographs of free standing grains from Group II 8 hour growths with (a) 1.5%, (b) 3% and (c) 4.5% $CH_4/H_2$ concentrations 15mm from center.

*Grain Size*

The grain sizes were found to decrease with increasing methane concentration, as seen by comparing the nearly equal thickness of the 1.5% and 4.5% samples. The grain size of the 3% sample was slightly higher, likely owing to its slightly greater thickness. Grain sizes and thicknesses were found to decrease slightly with radial distance from the center of the wafer. This is best understood by a inhomogeneous growth conditions, and a reduction of methane radicals towards the edges. Grain size was not included for the thick 4.5% sample, as it does not have well

defined features. These variations in grain sizes and thickness across the wafer were found not to produce a meaningful change in the texture index.

*Conclusions*

Texture analysis using the techniques of x-ray diffraction are presented and performed on diamond films grown by hot filament chemical vapor deposition on silicon under varying methane concentrations and thicknesses. The grain size is known to vary across the growth wafer, and the variation in grain size for each sample was analyzed for its effect on the texture. It is shown that higher methane concentrations lead to a higher <110> texture as evidenced by the Group II samples. Higher methane concentrations also was associated with a higher twinning density and reduction in grain size. The emergence of <110> texture from a nearly random distribution was shown to depend strongly on thickness in the case of the 4.5% samples.

It is found that the (311) pole figures were not suitable for texture analysis due to the appearance of underlying silicon peaks, and the generally low intensities from this Bragg condition. A different choice of substrate material, or thicker diamond samples may lead to a larger set of usable pole figures thereby increasing the accuracy of the estimated ODF. Pole figures from the lowest methane concentration, 1.50%, are shown below before (Figure 24) and after (Figure 252) removal of substrate peaks. It is suggested that the outlier removal was unsuccessful to the close proximity of the silicon peaks in the (311) pole figure.

For applications that depend on the lengths of the crystal domains or grain sizes, such as thermal conductivity, lower methane concentrations are recommended as the films produced have large features with the lowest density of twinning.

The CVD reactor was found to have minor inhomogeneities across the growth surface, possibly attributed to differences in methane radical availability. The effect of these inhomogeneities were not found to produce a meaningful change in the calculated orientation distribution.

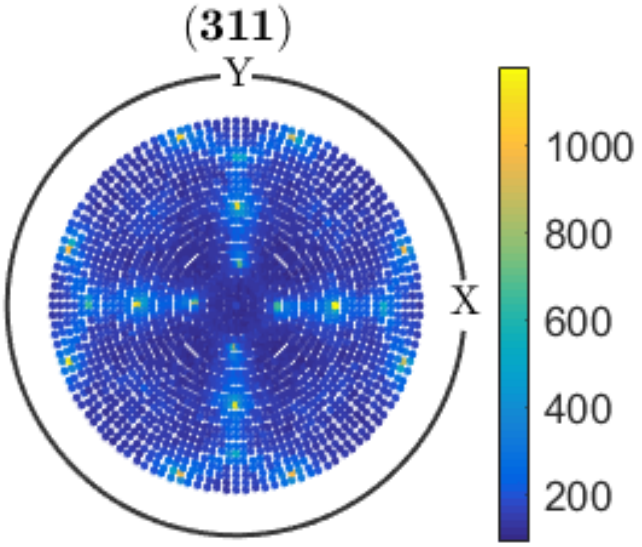


**Figure 24:** Pole figures of 1.5% methane sample before outlier removal.

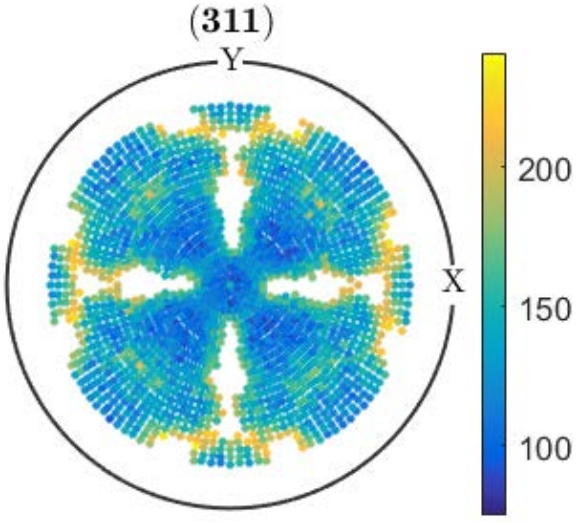


**Figure 25:** Pole figures of 1.5% methane sample and after outlier removal.

## LITERATURE CITED


[1] Prelas M A, Popovici G, Bigelow L K., Handbook of Industrial Diamonds and Diamond Films, New York: Marcel Dekker Press, (1998)

[2] Mario Birkholz, Paul F. Fewster, Christoph Genzel, *Thin Film Analysis by X-ray Scattering*, Wiley-VCH (2005)

[3] Y. Avigal, O. Glozman, I. Etsion, et al., *[100]-Textured diamond films for tribological applications*, Diamond Relat. Mater (1997)

[4] Su Q F, Xia Y B, Wang L J, et al., *Influence of texture on optical and electrical properties of diamond films,* Vacuum, **81**, 5 (2007)

[5] McCurdy, A K. , Physical Review B, **26**, 12 (1982)

[6] McCurdy A K, Maris H J, Elbaum C., *Anisotropic heat conduction in cubic crystals in the boundary scattering regime*, Physical Review B, **2**, 10 (1970)

[7] H. J Bunge, *Texture Analysis in Materials Science*, Butterworths, London (1982)

[8] K. Nagao and E. Kagami, "X-Ray Thin-Film Measurement Techniques VII. Pole Figure Measurement," Rigaku Journal, Vol. **27**, No. 2, (2011)

[9] R. J. Roe ,Description of crystallite orientation in polycrystalline materials. J Appl Phys., **36**, 2024 (1965)

[10] R.O. Williams, J. Appl. Phys., **39**, 4329 (1968)

[11] R.O. Williams, Trans Metall Soc AIME, (1968)

[12] S. Suwas, R.K Ray, *Crystallogrpahic Texture of Materials*, Springer London (2014)

[13] M. J. Buerger, Proc. Nat. Acad. Sci. U.S., **26**, 637 (1940)

[14] C. N. Tomé, H.-R. Wenk, U. F. Kocks, *Texture and Anisotropy: Preferred Orientations in Polycrystals and Their Effect on Materials Properties*, Cambridge University Press (1998)

[15] T. Liu, D. Raab, W. Maio, S. Zaefferer, Adv. Funct. Mater. **19** (2009) 3880-3891

[16] C. Wild, N. Herres and P. Koidl, J. Appl. Phys., **68**, 3 (1990)

[17] A. van der Drift, Philips Res. Rep., **22**, 267 (1967)

[18] L. Chen, W.M. Mao, H.P. Feng, F. X. Lu, Solid State Phenomena, **105**, 421 (2005)

[19] D. G. Goodwin, J. E. Butler, Handbook of Industrial Diamonds and Diamond Films, **6**, 527 (1998)

[20] M. Tsuda, M. Nakajima, S. Oikawa, J. Am. Chem. Soc., **108**, 5780 (1986)

[21] D. Meakin, J. Stoemenos, D. Miglierate, N. A. Economan, J. Appol. Phys., **61**, 5031 (1987)

[22] R.E. Clausing, L Heatherly, L. L. Horton, E.D. Specht, G. M. Begun, Z. L. Wang, Diamond and Related Materials, **1**, 411 (1992)

[23] E. Titus, D. Misra, M. Singh, et al., Journal of Materials Research, **19**, 3206 (2004)

[24] I. Schmidt, C. Benndorf, Diam. Relat. Mater., **10**, 347 (2001)

[25] K. Kobashi, S. Miyauchi, K. Nishimura, K. Kumagai, R. Kato, US patent 5358 754 (1994)

[26] H. X. Zhu, W. M. Mao, H. P. Hong, F. X. Lu, I. I. Vlasov, V. G. Ralchenko,A. V. Khomich, J. Inorg. Mater, **22**, 570 (2007)

[27] B. E. Williams, H. S. Kong, J. T. Glass, J. Mater. Res., 5, 801 (1990)

[28] C. S. Yan, K. Yogesh, M. N. Vohra, Diam. Relat. Mater., 8, 2022 (1999)

[29]Williams RO (1968) Analytical methods for representing complex textures by biaxial pole figures. J Appl Phys 39:4329–4335

[30] Matthies S, Vinel GW (1982) "An example demonstrating a new reproduction method of the ODF of texturized samples from reduced pole figures." Physica Status Solidi (B) 112:115–120

[31] Ruer D, Baro R (1977) "Vectorial method of texture analysis of cubic lattice polycrystalline material." J Appl Crystallogr 10:458–464

[32] Helming K, Eschner T (1990) "A new approach to texture analysis of multiphase materials using a texture component model". Crys Res Tech 25:203–208

[33] Creuziger A., Syed K., Gnäupel-Herold T., "Measurement of uncertainty in orientation distribution function calculations", Scripta Materialia, (2014)

[34] K.G. van den Boogaart, R. Hielscher, J. Prestin and H. Schaeben: Journal of Computational and Applied Mathematics Vol. 199 (2007), p. 122

[35] Bachmann F, Hielscher R, Schaeben H. Solid State Phenom, 160, 63 (2010)

[36] R. Hielscher and H. Schaeben: J. Applied Crystallography, Vol. 41, 1024, (2008)

[37] Bunge HJ, Esling C (1979) "Determination of the odd part of the texture function. J Phys Lett, 40:627–628

[38] Esling C, Bechlerferry E, Bunge HJ (1981) Numerical-calculation of the odd part of the texture
function. J Phys Lett 42:141–144

[39] Van HP (1983) The use of a quadratic form for the determination of nonnegative texture functions. Textures Microstruct 6:1–19

[40] Dahms M, Bunge HJ (1988) A positivity method for the determination of complete orientation
distribution functions. Textures Microstruct 10:21–35

[41] Dahms M, Bunge HJ (1989) The iterative series-expansion method for quantitative texture analysis.1. Gen Outline J Appl Crystallogr 22:439–447

[42] Wang F, Xu JZ, Liang ZD (1989) Determination of the ODF of hexagonal symmetry materials
according to the maximum-entropy method. Textures Microstruct 10:217–226

[43] D.I. Nikolayev et al., Mater. Sci. Forum, Vols. 495–497, 307 (2005)

[44] T.A. Lychagina, D.I. Nikolayev, F. Wagner, Texture, Stress, and Microstructure, Hindawi Publishing Corporation, Vol. 2009, pp. 1-10 (2009)

[45] S. Matthies, H.-R. Wenk, G.W. Vinel, J. Appl. Crystallogr., 21, 285-304 (1988)

[46] E. Heyn, The Metallographist, Vol. 5, 1903, pp. 39-64.